Deciphering the state of the lower crust and upper mantle with multi-physics inversion

Max Moorkamp[1]

[1]Ludwig-Maximilians-Universität, Department of Earth and Environmental Sciences, Theresienstrasse 41, 80333 Munich, Germany

Key Points:

- I present a new multi-physics based model of the western United States
- The physical paramaters are coupled through a newly developed variation of information constraint
- The models suggests that previous interpretations of the state of the lower crust are overly simplified and need to be revised

Corresponding author: Max Moorkamp, `Max.Moorkamp@lmu.de`

Abstract

The composition of the lower crust is a key factor in understanding tectonic activity and deformation within the Earth. In particular, the presence or absence of melt or fluids has strong control on tectonic evolution. Multi-physics inversion results from the western United States demonstrate that tectonic inheritance plays a much stronger role in determining the location of melt in the lower crust than previously thought. Even in a currently active area such as the Yellowstone Hotspot, fluid dominated structures and fluid free regions are juxtaposed. This is incompatible with the commonly used model of recent tectonic activity as a main controlling factor for the presence of fluids or melt. These results have global implications for how geophysical models are interpreted and how they can be related to geodynamic simulations.

1 Plain Language Summary

The majority of knowledge about the state of the Earth comes from the interpretation of geophysical surveys. However, these surveys give results in terms of physical parameters, e.g.electrical conductivity, and the relationship to phenomena of interest, e.g. the amount of molten material at depth, is often ambiguous. I combine different geophysical measurements with a new method derived from medical imaging to reduce this ambiguity. Results from the western United States with this new method indicate that the way scientists so far inferred melt content, for example, is overly simplified. It was thought that in geologically young and active regions melt was wide-spread, while older and stable regions were melt free. Instead this study shows a more complex picture where geologic history determines the location of molten material in addition to current geologic activity. This will require a thorough revision of previous results not only in the United States but around the globe.

2 Introduction

The origin of low resistivity within the crust and upper mantle has been debated for more than five decades (Hyndman & Hyndman, 1968; Frost et al., 1989) since early electromagnetic observations revealed low resistivities at depths of 10-40 km within the Earth (Schmucker, 1964). Since then large scale array measurements and modern analyses based on two-dimensional and three-dimensional inversion of magnetotelluric (MT) data have shown that low resistivities at these depths are a widespread feature both in tectonically active (Wei et al., 2001; Meqbel et al., 2014) as well as stable continental regions (Robertson et al., 2016; Moorkamp et al., 2019) possibly with the exception of some Archean cratons (Jones & Ferguson, 2001). However, based on electrical resistivity alone it is not possible to infer the origin of these features as all potential causes currently under consideration: saline fluids, melt, graphite and sulphides can produce comparable resistivity anomalies (Jones, 1992). Therefore other geophysical observations and petrological considerations must be taken into consideration to determine the cause of low resistivity in the lower crust. For example, saline fluids and melt produce an observable low velocity anomaly in seismological models and qualitative comparisons between these methods have been used to infer fluids and melt in Tibet (Wei et al., 2001). Where such data are not available, general considerations based on regional heat flow and the tectonic setting have been used to argue the case for fluids (Li et al., 2020), melt (Heise et al., 2007), graphite (Robertson et al., 2016) or sulphides (Rao et al., 2007). This ancillary information has largely been used in a qualitative way and thus might not reflect the true complexity and heterogeneity within the Earth. In particular, such qualitative lines of reasoning are difficult to test quantitatively.

3 Introduction

The north-western United States is a region of particular interest, as here active tectonics such as the subduction of the Juan de Fuca Plate, hotspot volcanism and active extension are juxtaposed against old lithosphere of the Wyoming craton and Colorado Plateau (Meqbel et al., 2014). Previous studies of the region have found wide-spread low-resistivity structures in the lower crust (Kelbert et al., 2012; Meqbel et al., 2014; Bedrosian & Feucht, 2014). Given the aforementioned difficulties in identifying the cause of the low resistivity, these structures are attributed to reflect fluids and melts in the active western region and around Yellowstone and to graphite (Meqbel et al., 2014) or sulfides (Bedrosian & Feucht, 2014) in cratonic regions. Expanding on this idea, Liu and Hasterock (Liu & Hasterok, 2016) construct a viscosity model along a profile from the Basin and Range to the Colorado Plateau where they associate low resistivity with low viscosity to perform simulations of lithospheric deformation and mantle flow. Their model successfully predicts various critical parameters including surface topography and highlights an avenue from static geophysical images to dynamic tectonic models, but critically hinges on the assumption that low resistivity in the crust corresponds to a zone of rheological weakness. While this is plausible for low resistivity caused by fluids, it might not be appropriate for a solid conductive phase (Selverstone, 2005).

Joint inversion of different geophysical data provides a quantitative approach to create multi-parameter models of the Earth (Moorkamp, 2017) and investigate the predictions made by the resulting model through sensitivity analyses. The presence of interconnected liquids such as saline fluids and melts results in low velocities, as mentioned above, but also in low bulk densities associated with the low resistivity structures due to the significantly lower density of the fluid components. In contrast, solid conductive phases such as graphite and sulphide have densities that are comparable to those of crustal rocks or even exceed them (Bellefleur et al., 2015). The combination of gravity measurements with magnetotelluric data to investigate the lithosphere is particularly attractive as global geodetic models exist that combine satellite and terrestial data and provide high-quality coverage for large parts of the globe (Pail et al., 2018).

4 Multi-physics inversion

I therefore combine long-period magnetotelluric (MT) data from the north-western United States (Kelbert et al., 2018) with satellite gravity measurements (Pail et al., 2018) in order to investigate the causes of low-resistivity in this region. I use the joint inversion framework jif3D (Moorkamp et al., 2011) with a newly developed resistivity-density coupling criterion based on variation of information (VI) (Moorkamp, 2021). VI is an unsupervised machine-learning method which constructs, where possible, a one-to-one relationship of a-priori unspecified form between the properties under consideration(Haber & Holtzman Gazit, 2013; Mandolesi & Jones, 2014), in this case density and resistivity. Within the multi-physics inversion the misfit for the two data-sets under consideration as well as the VI constraint are minimized simultaneously, i.e. the algorithm seeks a combined resistivity-density model that fits all observations and also shows maximum correspondence between the two physical properties.

Details about the multi-physics inversion software *jif3D* including the algorithms to solve the forward problem can be found in (Moorkamp et al., 2011). I therefore give only a brief summary of the main constituents and instead focus on the coupling through variation of information which has only been described briefly so far (Moorkamp, 2021). To construct the final combined density and resistivity model, the inversion solves a non-linear optimization problem with an objective function that consists of the data misfit for the magnetotelluric and gravity observations, regularization terms for the conductivity and density models, respectively, and the VI based coupling term. It employs an iterative non-linear optimization method based on a limited memory quasi-Newton method (L-BFGS) (Avdeeva & Avdeev, 2006) with forward engines based on an integral equation approach for magnetotellurics (Avdeev et al., 1997) and a massively parallel implementation for the gravity forward problem (Moorkamp et al., 2010). To ensure that conductivity and density remain within specified limits, the physical parameters are transformed to generalized parameters using the transform described in (Moorkamp et al., 2011) and the inverse problem is solved in this generalized parameter space. The two regularization terms are based on first-order forward differences to ensure smoothness of the model and reduce the influence of noisy measurements. I start the inversion with a large regularization parameter and successively relax the regularization until the inversion has converged to a data misfit comparable with the misfit for inversions based on each dataset individually. More information about the evolution of the different terms of the objective function and a comparison with individual inversions can be found in the supporting information.

Variation of information is an information theoretical measure of the amount of information contained in variable $\mathbf{x}$ about another variable $\mathbf{y}$ and closely related to the concept of Mutual Information (Mandolesi & Jones, 2014). It is widely used in medical imaging (Pluim et al., 2003) and climate science (DelSole et al., 2013), but so far has not been used in multi-physics imaging. To couple resistivity and density within the inversion framework, variation of information is minimized. This will result in models where, if possible, each density value corresponds to a unique resistivity value without prescribing a particular shape of that relationship. As it is provided as a term of the objective function in the inversion, this one-to-one relationship can be violated if mandated by the data to achieve a satisfactory fit.

To calculate the variation of information between conductivity and density I use a kernel density approach with a Gaussian kernel. However, the variation of information is not calculated on the quantities themselves, but on the generalized model parameters described above. This has the advantage that the input quantities are dimensionless and have comparable mean and variance. The first step in calculating VI is estimating the probability density distribution (pdd) for the joint parameters and the marginal distributions for each parameter. Denoting the pairs of transformed parameters in each model cell as (x_i, y_i) where $i = 1 \dots M$ and M is the number of cells used to discretize the inverse problems, the pdd is approximated as

$$p(\xi_j, \eta_k) = \frac{1}{2\pi M} \sum_{i=1}^{M} \exp\left(\frac{(x_i - \xi_j)^2 + (y_i - \eta_k)^2}{\sigma^2}\right).$$

Here ξ_j and η_k are the discrete values at which we wish to approximate the pdd. For this study I use $N = 100$ evenly spaced values across the expected parameter range for each parameter and choose the standard deviation of the Gaussian, σ, as half the discretization width. From the joint pdd we can also calculate the marginal pdd's $p(\xi_j) = \sum_k p(\xi_j, \eta_k)$ and $p(\eta_k) = \sum_j p(\xi_j, \eta_k)$. In a second step we then calculate the Shannon Entropy $H(\mathbf{x}) = -\sum_i p(x_i) \log p(x_i)$ of the marginal and joint pdd's and finally retrieve the variation of information as

$$VI(\mathbf{x}, \mathbf{y}) = 2H(\mathbf{x}, \mathbf{y}) - H(\mathbf{x}) - H(\mathbf{y}).$$

The calculated variation of information is added to the inversion as a term in the objective function and thus minimized.

To use VI in an optimization context, we also need to calculate the partial derivatives with respect to the model parameters, i.e. $\frac{\partial VI}{\partial \mathbf{x}}$ and $\frac{\partial VI}{\partial \mathbf{y}}$. This can be performed analytically by calculating the respective derivatives for the Gaussian kernel and applying the chain rule to account for the Entropy calculation. For example, we have

$$\frac{\partial H(\mathbf{x})}{\partial x_i} = \sum_{i=1}^{M} \sum_{i=j}^{M} \frac{(x_i - \xi_j)}{2\pi M \sigma^2} \sum_{i=1}^{M} \exp\left(\frac{(x_i - \xi_j)^2 + (y_i - \eta_k)^2}{\sigma^2}\right),$$

and similarly for the other derivatives. Once the partial derivatives for entropy have been calculated, the derivative for VI can be calculated as a simple linear combination.

For the inversion an error floor of 2% of the maximum absolute value of impedance in each row of the impedance tensor for the MT data and 1-10 mGal for the gravity data based on the difference between a spherical approximation and a flat Earth approximation are assumed. With these uncertainty estimates, the inversion fits both datasets to RMS values of 1.9 (Gravity) and 1.6 (MT), respectively. These value are comparable to individual inversions of each dataset and, for MT, the model of Meqbel et al. (2014). More information on the chosen errors, data fits and model assumptions can be found in the Supplementary Material.

5 Integrated model of the western United States

Figure 1 shows horizontal slices through the resulting joint resistivity-density model at depths of 30 km and 100 km which correspond to the base of the crust and the base of the lithosphere, respectively. The resistivity structure is generally consistent with previous models with enhanced definition of individual features (cf. Supplementary material). This is particularly evident at 100 km where the Juan de Fuca Slab and the Siletzia Slab Curtain (Schmandt & Humphreys, 2011) are imaged as sharp discrete features, but appear as broad resistive regions in models based on MT alone (Meqbel et al., 2014). Also note the remarkable coincidence between the western edge of the resistive feature associated with the Juan de Fuca Slab and the prediction made by the Slab2 model (Hayes et al., 2018) (dashed line in Figure 2). Within the mantle, several isolated conductive features can be observed which are consistent in location and shape with previously imaged features that have been interpreted as signatures of melt and slab-derived fluids (Meqbel et al., 2014). The mantle density model shows a strong correspondence to the resistivity model. Resistive features such as the active and remnant slabs are imaged as high density anomalies as expected and conversely low resistivity is associated with low density consistent with an interpretation of enhanced fluid content.

At 30 km depth, within the lower crust, the model shows low resistivities in large parts of the region, particularly in the tectonically active Basin and Range Region in the southern and western part of the model. East of 110° W, towards the older shield regions, only isolated conductors are imaged. On the large scale low resistivities correlate with negative density anomalies as discussed for the mantle above. However, in some areas we can identify deviations from this simple correlation. For example, the northern part of the Snake River Plain (SRP) shows significant regions where low resistivities correspond to high densities. To illustrate this further I show a vertical slices through some of these anomalies in Figure 2.

The resistivity model (Figure 2) shows a series of low resistivity structures in the lower-most crust and upper-most mantle. The lateral boundaries of these structures generally coincide with boundaries between distinct physio-geographic regions. In all cases we can identify corresponding anomalies in the density model, however some of these show lower density than the background and others show higher densities than the background. It is important to note in this context that the VI constraint used to couple the two models aims at associating each resistivity value with a unique density value. Thus these different associations of high and low density with low resistivity values directly contradict the coupling constraint and thus are required by the data.

6 Density-resistiviy relationships

In order to investigate this observation further, the density-resistivity relationship for each cell in our joint model is plotted in Figure 3. The bulk of the estimates is located on a tight s-shaped curve. This shape has not been prescribed a-priori but evolves data-driven through the VI-constraint in the inversion. Outside the main spine of this relationship we observe some scatter related to heterogeneous near-surface structure but, more importantly, two leg-shaped features with near constant density and low resistivities between 0.5-20 Ωm. One of these (marked as high-density conductor in Figure 3) represents relatively dense and conductive material in the crust. It is close to neutrally bouyant and an increase in conductivity does not lead to a significant change in density. This suggests that the causative material for this structure has a similar density to the host rock and the most likely explanations are sulfide or graphite. In contrast, the low density conductor (see Figure 3) at this depth shows a decrease in density with descreasing resistivity, i.e. the conductive material has a density significantly smaller than the host rock. In fact, the observed relationship is broadly compatible with predictions of density and conductivity based on a modified Archie's law (Glover et al., 2000) (black line in Figure 3). For this calculation, I assume a density contrast of -2000 kg/m^3 and a conductivity of 50 S/m for the conductive phase as typically assumed for crustal fluids (Jones, 1992). These first-order calculations are not suitable for quantitative interpretation of fluid fraction, but demonstrate the consistency of the data derived estimates with petrophysical considerations.

The locations of high-density, i.e. corresponding to a solid conductive phase (blue), and low density, corresponding to a fluid conductive phase(red), conductive structures in the depth range between 28 and 39 km are summarized in Figure 4. Large parts of the region show conductive structures that are compatible with a fluid origin, e.g. in the active Basin and Range province. However, fluid derived conductors are also identified along the assumed limits of the Wyoming Craton to the north east. Conversely, solid phase based conductive structures are found in the northern Snake River Plain and in close proximity to Yellowstone (marked by a yellow star in Figure 4). Although these solid phase conductors make up only a small volume of the observed conductive structures, the pattern is not random. There is a strong correlation with the northern boundary of the Snake Rive Plain and the transition from solid to fluid caused conductivity is strongly related to physio-geographic boundaries. A possible explanation is that this is the signature of a suture zone similar to those inferred further north(Meqbel et al., 2014).

7 Implications for global interpretations

These results clearly demonstrate that the simple association of young and active tectonic areas with fluid caused conductivity and old regions with solid caused conductivity currently employed in the literature cannot be maintained. Rheological modelling (Liu & Hasterok, 2016) was performed in the south-eastern part of our study areas where our results are compatible with the assumed fluid derived conductivity. However, had this analysis been performed further to the north, this assumption would not hold. I have shown here how different causes of conductivity in the crust and mantle can be distinguished and these our results require a new interpretation of the conductivity structure not only in the western United States but globally. For example, applying a similar multi-physics analysis to Tibet, where wide-spread fluids have been inferred based on electrical conductivity models(Wei et al., 2001), could potentially alter our understanding of the causes of low resistivity and result in different inferences on its geodynamics (Bai et al., 2010). Global application would mark an important step in understanding the composition of the lower crust and linking geophysical images to models of lithospheric dynamics. Beyond this there is a wealth of additional information in the multi-physics models and the corresponding parameter relationships that I have not been able to discuss here. Thus these results are only the beginning of a new era of lithosphetic imaging.

Acknowledgments

This work was funded by the German Research Foundation, DFG, under grant MO 2265/4-1 and by the European Space Agency ESA as part of the Support to Science Element 3D Earth. Alan G. Jones and Graham J. Hill provided helpful comments on an early version of the manuscript. Bernhard Weise provided the processed gravity data.

The gravity data have been extracted from the global XGM2016 gravity model (Pail et al., 2018) which is accessible at `http://doi.org/10.5880/icgem.2017.003`. Grids for our study region can be obtained through the ICGEM calculation service `http://`

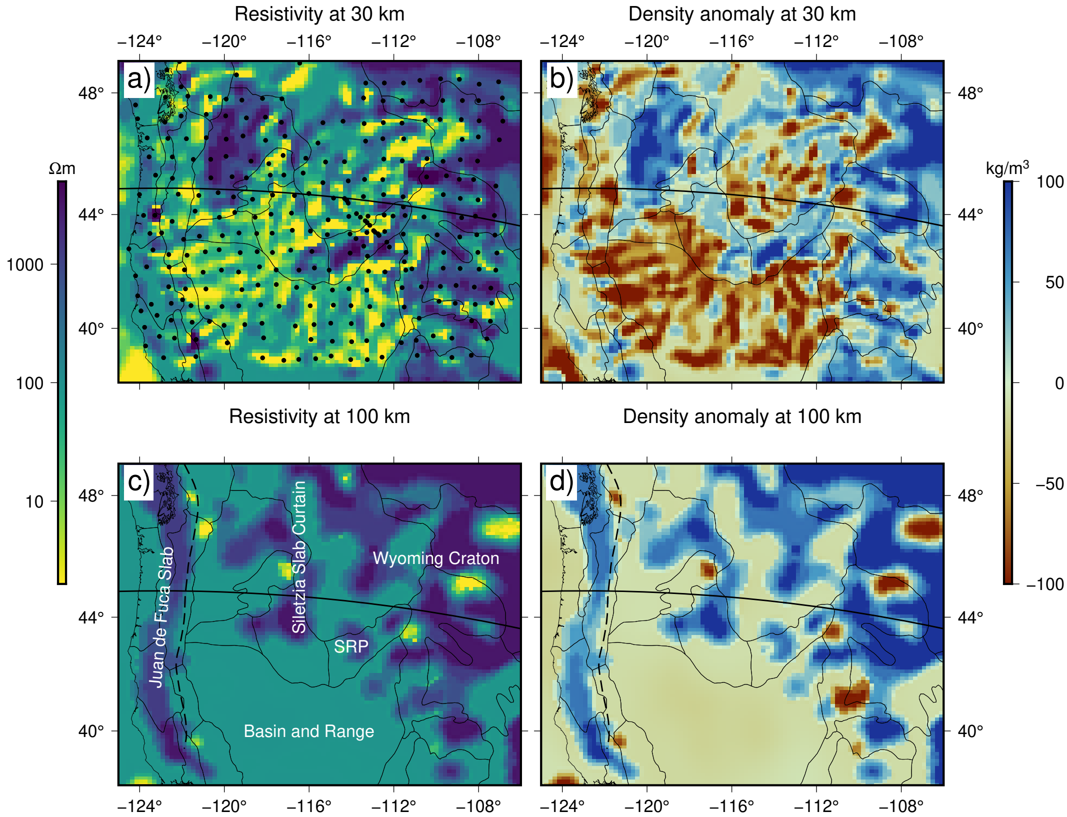

Figure 1. Horizonal slices through our integrated resistivity-density models at depths of 30 km (top row) and 100 km (bottom row). The locations of the MT sites used for the inversion are shown in panel a) The solid black line indicates the surface trace of the vertical profiles in Figure 2. The dashed line in panels b) and d) shows the boundary of the Juan de Fuca slab in the Slab2 model(Hayes et al., 2018). Also shown are the boundaries of the physiographic divisions (Fenneman & Johnson, 1946).

`icgem.gfz-potsdam.de/tom_longtime` by selecting XGM2016 (model 161) and calculating the free-air anomaly (gravity_anomaly_cl). The magnetotelluric measurements have been acquired as part of the USArray Lithoprobe program and can be downloaded at `https://ds.iris.edu/spud/emtf`. The inversion codes used for this study can be obtained via subversion (`https://subversion.apache.org`) at `svn checkout https://svn.code.sf.net/p/jif3d/jif3dsvn/trunk/jif3D jif3d`. Processed data and model files can be found in the Supporting Information as well as `https://doi.org/10.5281/zenodo.5535731`.

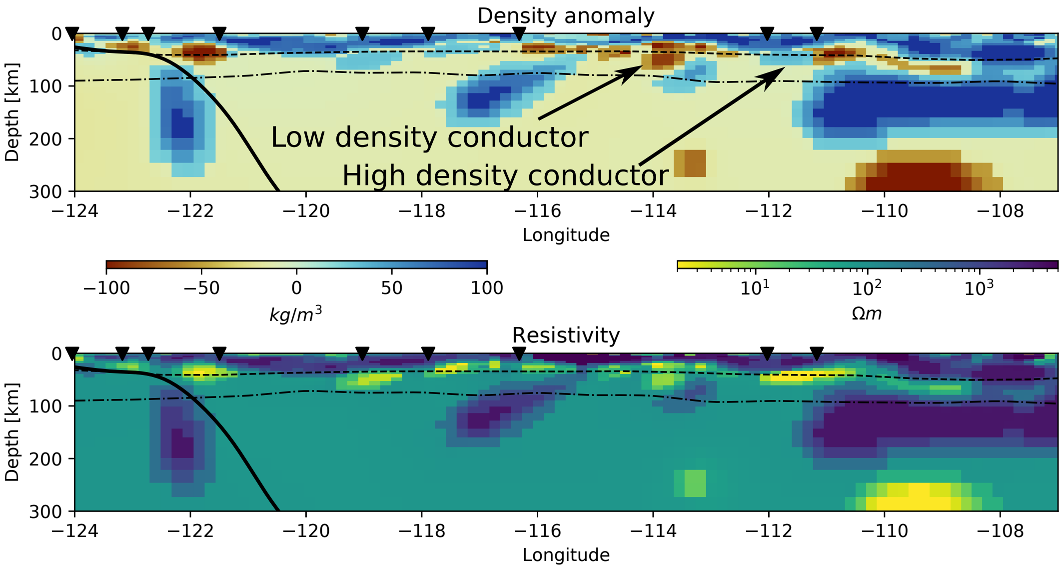

Figure 2. Vertical slices through the integrated model along the profile shown in Figure 1. Intersections with the physiographic divisions are marked with black inverted triangles. The thick black line shows the slab boundary from Slab2(Hayes et al., 2018). The Moho (dashed line)(Szwillus et al., 2019) and the negative wave-speed disconinuity (NVD, dot dashed line)(Liu & Gao, 2018) are also shown.

References

Avdeev, D. B., Kuvshinov, A. V., Pankratov, O. V., & Newman, G. A. (1997). High-performance three-dimensional electromagnetic modeling using modified Neumann series. Wide-band numerical solution and examples. *Journal of Geomagnetism and Geoelectricity*, *49*, 1519–1539.

Avdeeva, A., & Avdeev, D. (2006). A limited-memory quasi-newton inversion for 1d magnetotellurics. *Geophysics*, *71*(5), G191–G196.

Bai, D., Unsworth, M. J., Meju, M. A., Ma, X., Teng, J., Kong, X., … others (2010). Crustal deformation of the eastern tibetan plateau revealed by magnetotelluric imaging. *Nature geoscience*, *3*(5), 358–362.

Bedrosian, P. A., & Feucht, D. W. (2014). Structure and tectonics of the northwestern united states from earthscope usarray magnetotelluric data. *Earth and Planetary Science Letters*, *402*, 275–289.

Bellefleur, G., Schetselaar, E., White, D., Miah, K., & Dueck, P. (2015). 3d seismic imaging of the lalor volcanogenic massive sulphide deposit, manitoba, canada.

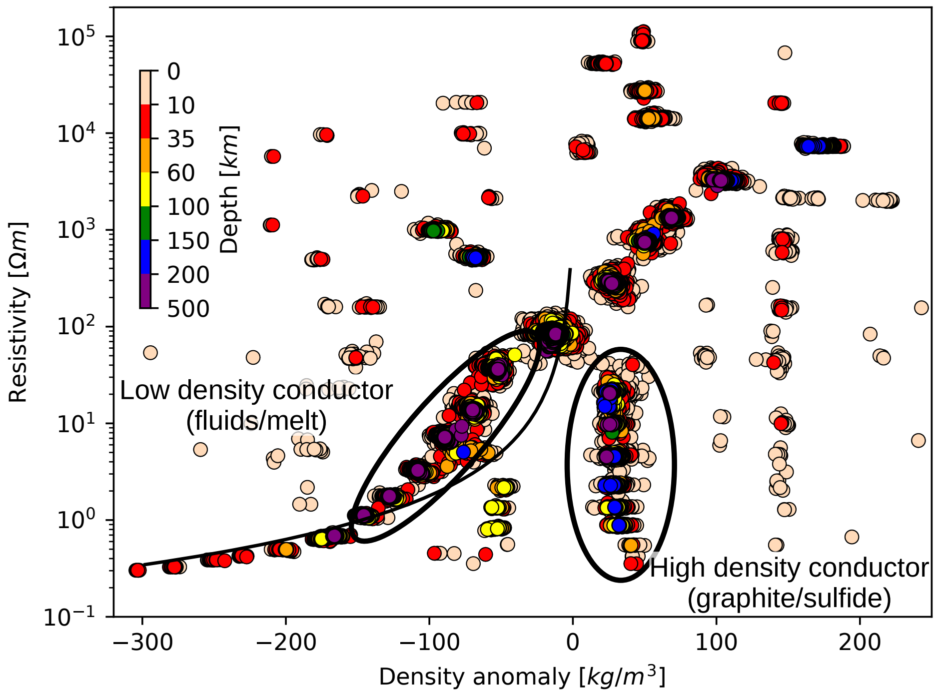

Figure 3. Resistivity vs. density relationship extracted from the integrated inversion model. Each dot is coloured by its corresponding depth. The black line shows the predicted density-resistivity relationship based on a fluid with a density contrast of -2000 kg/m^3 and a conductivity of 50 S/m assuming a modified Archie's law(Glover et al., 2000).

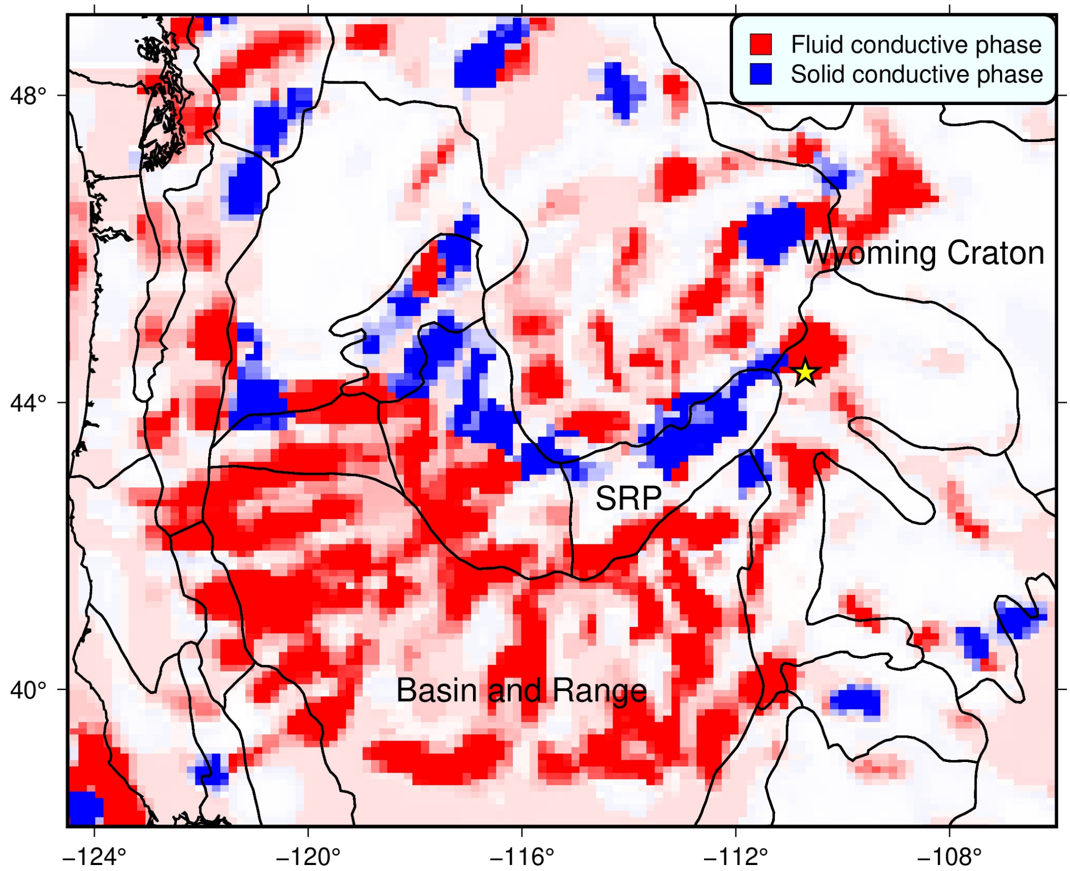

Figure 4. Conductive structures at depths between 28-39 km, corresponding to the lower crust and uppermost mantle, coloured by density anomaly. Red indicates below average density at this depth indicating a liquid conductive phase, blue indicates neutral to above average density, associated with a solid conductive phase. The location of the Yellowstone Hotspot is marked by a yellow star.

Geophysical Prospecting, *63*(4), 813–832.

DelSole, T., Kumar, A., & Jha, B. (2013). Potential seasonal predictability: Comparison between empirical and dynamical model estimates. *Geophysical Research Letters*, *40*(12), 3200–3206. doi: 10.1002/grl.50581

Fenneman, N., & Johnson, D. (1946). Physiographic divisions.

Frost, B. R., Fyfe, W. S., Tazaki, K., & Chan, T. (1989). Grain-boundary graphite in rocks and implications for high electrical conductivity in the lower crust. *Nature*, *340*(6229), 134–136.

Glover, P. W., Hole, M. J., & Pous, J. (2000). A modified archie's law for two conducting phases. *Earth and Planetary Science Letters*, *180*(3-4), 369–383.

Haber, E., & Holtzman Gazit, M. (2013). Model fusion and joint inversion. *Surveys in Geophysics*, *34*(5), 675-695. doi: 10.1007/s10712-013-9232-4

Hayes, G. P., Moore, G. L., Portner, D. E., Hearne, M., Flamme, H., Furtney, M., & Smoczyk, G. M. (2018). Slab2, a comprehensive subduction zone geometry model. *Science*, *362*(6410), 58–61.

Heise, W., Bibby, H. M., Caldwell, T. G., Bannister, S. C., Ogawa, Y., Takakura, S., & Uchida, T. (2007). Melt distribution beneath a young continental rift: the taupo volcanic zone, new zealand. *Geophysical Research Letters*, *34*(14).

Hyndman, R., & Hyndman, D. (1968). Water saturation and high electrical conductivity in the lower continental crust. *Earth and Planetary Science Letters*, *4*(6), 427–432.

Jones, A. G. (1992). Electrical conductivity of the continental lower crust. *Continental lower crust*, 81–143.

Jones, A. G., & Ferguson, I. J. (2001). The electric moho. *Nature*, *409*(6818), 331–333.

Kelbert, A., Egbert, G., et al. (2012). Crust and upper mantle electrical conductivity beneath the Yellowstone Hotspot Track. *Geology*, *40*(5), 447–450.

Kelbert, A., Erofeeva, S., Trabant, C., Karstens, R., & Van Fossen, M. (2018). Taking magnetotelluric data out of the drawer. *EOS*, *99*. doi: 10.1029/2018EO112859

Li, X., Ma, X., Chen, Y., Xue, S., Varentsov, I. M., & Bai, D. (2020). A plume-modified lithospheric barrier to the southeastward flow of partially molten tibetan crust inferred from magnetotelluric data. *Earth and Planetary Science Letters*, *548*, 116493.

Liu, L., & Gao, S. S. (2018). Lithospheric layering beneath the contiguous united states constrained by s-to-p receiver functions. *Earth and Planetary Science Letters*, *495*, 79–86.

Liu, L., & Hasterok, D. (2016). High-resolution lithosphere viscosity and dynamics revealed by magnetotelluric imaging. *Science*, *353*(6307), 1515–1519.

Mandolesi, E., & Jones, A. G. (2014). Magnetotelluric inversion based on mutual information. *Geophysical Journal International*, *199*(1), 242-252. doi: 10.1093/gji/ggu258

Meqbel, N. M., Egbert, G. D., Wannamaker, P. E., Kelbert, A., & Schultz, A. (2014). Deep electrical resistivity structure of the northwestern US derived from 3-d inversion of USArray magnetotelluric data. *Earth and Planetary Science Letters*, *402*, 290–304.

Moorkamp, M. (2017). Integrating electromagnetic data with other geophysical observations for enhanced imaging of the earth: a tutorial and review. *Surveys in Geophysics*, *38*(5), 935–962.

Moorkamp, M. (2021). Joint inversion of gravity and magnetotelluric data from the ernest-henry iocg deposit with a variation of information constraint. In *First international meeting for applied geoscience & energy* (pp. 1711–1715).

Moorkamp, M., Fishwick, S., Walker, R. J., & Jones, A. G. (2019). Geophysical evidence for crustal and mantle weak zones controlling intra-plate seismicity–the 2017 Botswana earthquake sequence. *Earth and Planetary Science Letters*, *506*, 175–183.

Moorkamp, M., Heincke, B., Jegen, M., Roberts, A. W., & Hobbs, R. W. (2011). A framework for 3-D joint inversion of MT, gravity and seismic refraction data. *Geophysical Journal International*, *184*, 477-493. doi: 10.1111/j.1365-246X.2010.04856.x

Moorkamp, M., Jegen, M., Roberts, A., & Hobbs, R. (2010). Massively parallel forward modeling of scalar and tensor gravimetry data. *Computers & Geosciences*, *36*(5), 680 - 686. doi: DOI:10.1016/j.cageo.2009.09.018

Pail, R., Fecher, T., Barnes, D., Factor, J., Holmes, S., Gruber, T., & Zingerle, P. (2018). Short note: the experimental geopotential model xgm2016. *Journal of geodesy*, *92*(4), 443–451.

Pluim, J., Maintz, J., & Viergever, M. (2003). Mutual-information-based registration of medical images: A survey. *IEEE Transactions on Medical Imaging*, *22*(8), 986-1004.

Rao, C. K., Jones, A. G., & Moorkamp, M. (2007). The geometry of the Iapetus Suture Zone in central Ireland deduced from a magnetotelluric study. *Physics of the Earth and Planetary Interiors*, *161*, 134-141. doi: 10.1016/j.pepi.2007.01.008

Robertson, K., Heinson, G., & Thiel, S. (2016). Lithospheric reworking at the proterozoic–phanerozoic transition of australia imaged using auslamp magnetotelluric data. *Earth and Planetary Science Letters*, *452*, 27–35.

Schmandt, B., & Humphreys, E. (2011). Seismically imaged relict slab from the 55 ma siletzia accretion to the northwest united states. *Geology*, *39*(2), 175–178.

Schmucker, U. (1964). Anomalies of geomagnetic variations in the southwestern united states. *Journal of geomagnetism and geoelectricity*, *15*(4), 193–221.

Selverstone, J. (2005). Preferential embrittlement of graphitic schists during extensional unroofing in the alps: the effect of fluid composition on rheology in low-permeability rocks. *Journal of Metamorphic Geology*, *23*(6), 461–470.

Szwillus, W., Afonso, J. C., Ebbing, J., & Mooney, W. D. (2019). Global crustal thickness and velocity structure from geostatistical analysis of seismic data. *Journal of Geophysical Research: Solid Earth*, *124*(2), 1626–1652.

Wei, W., Unsworth, M., Jones, A., Booker, J., Tan, H., Nelson, D., … others (2001). Detection of widespread fluids in the tibetan crust by magnetotelluric studies. *Science*, *292*(5517), 716–719.